5

Epitaxial $SrRuO_3$ Thin Films Deposited on SrO buffered-Si(001) Substrates for Ferroelectric $Pb(Zr_{0.2}Ti_{0.8})O_3$ Thin Films

Soon-Gil Yoon

School of Nano Science and Technology, Graduate of Analytical Science and Technology (GRAST), Chungnam National University, Daeduk Science Town, 305-764, Daejeon Korea

1. Introduction

At present there is considerable interest in utilizing ferroelectric thin films as a medium for non-volatile data storage [1]. In particular, much attention has been focused on investigating high density giga-bit data storage using scanning probe techniques [2]. It is known that the thickness of a 180° domain wall in ferroelectric thin film is 1-2 nm [3]. As such, these films have potential to serve as a medium for scanning probe microscopy (SPM)-based ultrahigh density (100 Gbit/cm^2 class) data storage [2]. It has been proposed that employing ferroelectric films as recording media inherently has several advantages: 1) the recorded data are non-volatile, 2) the recording density can be ultra high because of narrow domain wall thickness, 3) the ferroelectric domains can have fast switching speeds, and 4) information bits can be written and read electrically.

Among the various perovskite oxide materials, PZT films appear to be suitable as a storage medium, since their remanent polarizations are high. The highly tetragonal PZT films exhibit high remanent polarization showing a square-shaped hysteresis curve, compared with films having morphotropic and rhombohedral compositions. Therefore, $Pb(Zr_{0.2}Ti_{0.8})O_3$ films with a highly tetragonal structure are suitable for nano-data storage system applications. Ferroelectric $Pb(Zr_{0.2}Ti_{0.8})O_3$ thin films grown epitaxially on $SrRuO_3/SrTiO_3$ are reported to exhibit large P_r (remanent polarization) [4-5].

$SrRuO_3$ is a conductive oxide (a room temperature resistivity of 280 μΩ·cm for single crystals), pseudo-cubic perovskite with a lattice constant of 0.55 nm, and has a low mismatch with $Pb(Zr_{0.2}Ti_{0.8})O_3$(~ 0.5 %) and SrO (~ 1.7 %), thus allowing high quality epitaxial growth. Single-crystal epitaxial thin films of $SrRuO_3$ and $Sr_{1-x}Ca_xRuO_3$[6] are frequently grown on $SrTiO_3$ substrates. In order to achieve epitaxial growth of $SrRuO_3$ on Si, yttria-stabilized zirconia (YSZ) [7-8] and MgO [9] have been employed as buffer layer materials. Another promising candidate for the buffer layer is SrO which has a NaCl-type cubic structure with a lattice parameter of a = 5.140 Å [10-11]. The SrO(110) dielectric layer also exhibits good compatibility with Si(001) showing a low lattice mismatch of about 0.4 % [12].

In this study, highly tetragonal $Pb(Zr_{0.2}Ti_{0.8})O_3$ films were grown on epitaxial $SrRuO_3$ thin film electrodes using a SrO buffer layer on Si(001) substrates by pulsed laser deposition. The effect of the SrO buffer layer on the surface morphologies and the electrical properties of the

$SrRuO_3$ thin film electrodes was investigated as a function of SrO buffer layer thickness. Ferroelectric properties in c-axis oriented $Pb(Zr_{0.2}Ti_{0.8})O_3$ thin films deposited on an epitaxial $SrRuO_3$ electrode were also investigated.

2. Experimental procedure

The SrO target for pulsed laser deposition is difficult to make due to the low sinterability of SrO materials. A SrO_2 target was used to deposit SrO on Si (001) substrates in a vacuum ambient. Before deposition of SrO layers on Si (001) substrates, Si wafers were etched using HF solution to remove the native oxide layers. SrO, $SrRuO_3$ and PZT films were deposited on etched-silicon substrates using a KrF excimer laser (λ = 248 nm) with a maximum repetition rate of 10 Hz. Laser pulse energy density used for SrO, $SrRuO_3$ and PZT films deposited using ceramic targets was approximately 1.5 J/cm^2. 30 mol % excess PbO in the PZT targets was added to compensate for the PbO loss during both the sintering and deposition processes. The distance between the target and substrate was varied depending on the deposited materials. The typical SrO, $SrRuO_3$, and PZT deposition conditions are summarized in Table 1. The SrO, $SrRuO_3$, and PZT were in-situ deposited at each temperature in order to ensure chemical stability of the SrO films with Si. The PZT films were cooled down to room temperature at an oxygen pressure of 300 Torr to preserve the oxygen content in the films during the cooling procedure.

Deposition parameters	SrO	$SrRuO_3$	$Pb(Zr_{0.2}Ti_{0.8})O_3$
Target	SrO_2	$SrRuO_3$	$Pb(Zr_{0.2}Ti_{0.8})O_3$
Deposition temperature	700°C	550~750°C	575~600°C
Film thickness	3~30nm	50~300nm	100nm
Deposition pressure	1x10^{-6} Torr	1x10^{-2} Torr	1x10^{-1} Torr
Energy density	1.5 J/cm^2	1.5 J/cm^2	1.5 J/cm^2
Repetition rate	1 Hz	10 Hz	10 Hz
Target-substrate distance	3 cm	4 cm	6 cm
Substrates	Si (001)	SrO/Si	$SrRuO_3$/SrO/Si

Table 1. Deposition conditions of $Pb(Zr_{0.2}Ti_{0.8})O_3$ thin films, $SrRuO_3$ electrodes, and SrO buffer layers on Si (001) substrates by pulsed laser deposition

The surface morphologies of $SrRuO_3$ and PZT were characterized by atomic force microscopy (AFM, AUTOPROBE CP, PSI). Crystalline properties of the films were investigated by θ–2θ, ω-scan, and Φ-scan using a high resolution X-ray diffraction (HRXRD, Rigaku RINT2000). The composition of the $SrRuO_3$ films was identified by Rutherford backscattering spectroscopy (RBS) using a beam energy of 2.236 MeV ($4He^{++}$) and an incident angle of 160^o. The elemental distribution in the PZT/$SrRuO_3$/SrO/Si structure was investigated by secondary ion mass spectroscopy (SIMS) and Auger electron spectroscopy (AES). The resistivity of $SrRuO_3$ thin films was measured by an electrometer (CMT-SR 1000) using a four-point probe. The ferroelectric properties and leakage current characteristics were measured using a RT66A ferroelectric tester (Radiant Technology) operating in the virtual ground mode and a Keithley 617 electrometer, respectively. The measurements were carried out using a metal–insulator–metal (MIM) configuration. A Pt top electrode (Area = 7.85×10^{-5} cm^2) patterned using lift-off lithography was prepared at room temperature by dc sputtering.

3. Results and discussion

Figure 1(A) shows XRD patterns of 100 nm thick-$SrRuO_3$ thin films deposited on SrO buffer layers with various thicknesses. The XRD patterns were plotted using a log-scale to check the existence of the minor portion of SrO_2 phase within the $SrRuO_3$ films. The $SrRuO_3$ films were deposited at about 650°C in 1×10^{-2} Torr. As shown in Fig. 1(A), $SrRuO_3$ films deposited on 6 nm-thick-SrO buffered Si (001) substrates exhibit a c-axis preferred orientation, indicating the (001) and (002) planes alone. In the case of buffer layers above 12 nm thickness, SrO_2 phase was observed in the $SrRuO_3$ films. From the XRD results, the SrO buffer layer was found to play an important role for the preferred growth of $SrRuO_3$ films on Si substrates at below approximately 6 nm-thickness. In order to investigate the epitaxial relationship between $SrRuO_3$ and SrO(6 nm)/Si(001), a Φ-scan in the $SrRuO_3$/SrO/Si structure was performed and the results are shown in Fig. 1 (B). Peaks of $SrRuO_3$ {111} can be observed at every 90°, indicating that the $SrRuO_3$ films are epitaxially grown on a SrO/Si (001).

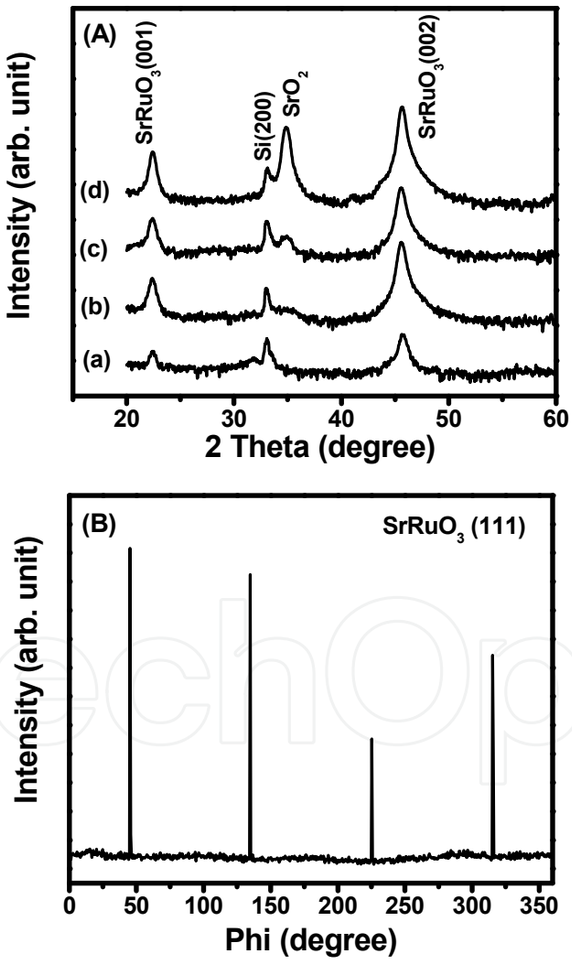

Fig. 1. (A) XRD patterns of 100nm thick-$SrRuO_3$ thin films deposited on SrO buffer layers of (a) 3 nm, (b) 6 nm, (c) 12 nm, and (d) 30 nm thickness. (B) Φ-scan profile of $SrRuO_3$ films deposited on SrO (6nm)/Si. (XRD patterns were plotted using a log-scale)

Figure 2 shows the variation in resistivity and rms roughness of 100nm thick-$SrRuO_3$ thin films as a function of SrO thickness. The $SrRuO_3$ films deposited on ultra-thin SrO films of about 3nm show the highest rms roughness and resistivity values because the SrO films do not play a role as a buffer layer. On the other hand, above 6nm thickness, $SrRuO_3$ films exhibit a low rms roughness of about 3-5 Å and a resistivity of 1700 – 1900 μΩ-cm. The resistivity values of the $SrRuO_3$ films deposited on 6nm-thick SrO buffer layers are approximately 1700 μΩ-cm, higher than that of $SrRuO_3$ films (~ 400 μΩ-cm) deposited on $SrTiO_3$ single crystals[13] and (100) $LaAlO_3$ single crystals[14]. The high resistivity of the $SrRuO_3$ films on Si substrates originates from the existence of silicon oxide formed from the diffusion of silicon, because the thin SrO layer does not prevent the diffusion of silicon during the deposition of $SrRuO_3$ at high temperature. The full-width-half-maximum (FWHM) values of the $SrRuO_3$ films deposited on SrO/Si and $SrTiO_3$ single crystal substrates are approximately 7.32° and 0.15°, measured by ω-scan, respectively. These results suggest that the $SrRuO_3$ films grown on Si substrates are inferior in terms of film qualities such as crystallinity and defects relative to those grown on $SrTiO_3$ single crystals. The inset in Fig. 2 shows three-dimensional AFM images of $SrRuO_3$ films deposited on (a) 3 nm thick- and (b) 30 nm thick-SrO buffer layers.

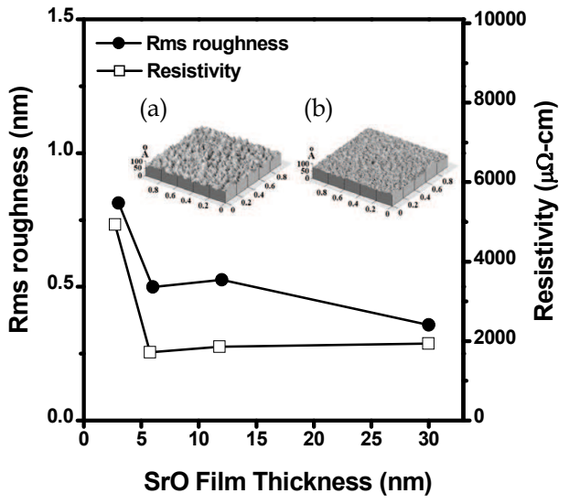

Fig. 2. Variation in resistivity and rms roughness of 100 nm thick-$SrRuO_3$ thin films as a function of SrO thickness. The inset shows three-dimensional AFM images of $SrRuO_3$ thin films deposited on SrO buffer layers of (a) 3 nm and (b) 30 nm thickness

Figures 3(a) and 3(b) show XRD patterns and rms roughness and resistivity of $SrRuO_3$ films, respectively, as a function of $SrRuO_3$ thickness. The $SrRuO_3$ films were deposited at 650°C on 6 nm thick-SrO buffer layers. As shown in Fig. 3(a), the peak intensity of $SrRuO_3$ {001} increases with increasing $SrRuO_3$ thickness, and the $SrRuO_3$ films of 50 nm thickness also exhibit a *c*-axis preferred relationship with Si(001) substrates. The resistivity of the $SrRuO_3$ films exhibits a constant value of about 1700 μΩ-cm irrespective of the film thickness above 50nm. The rms roughness of the $SrRuO_3$ films exhibits a similar tendency with the variation of resistivity as a function of $SrRuO_3$ thickness. The film roughness in conducting materials is inversely proportional to the mobility of the charge carriers. The resistivity in the conducting films is also inversely proportional to the mobility of the charge carriers if the concentration of the charge carriers is constant.

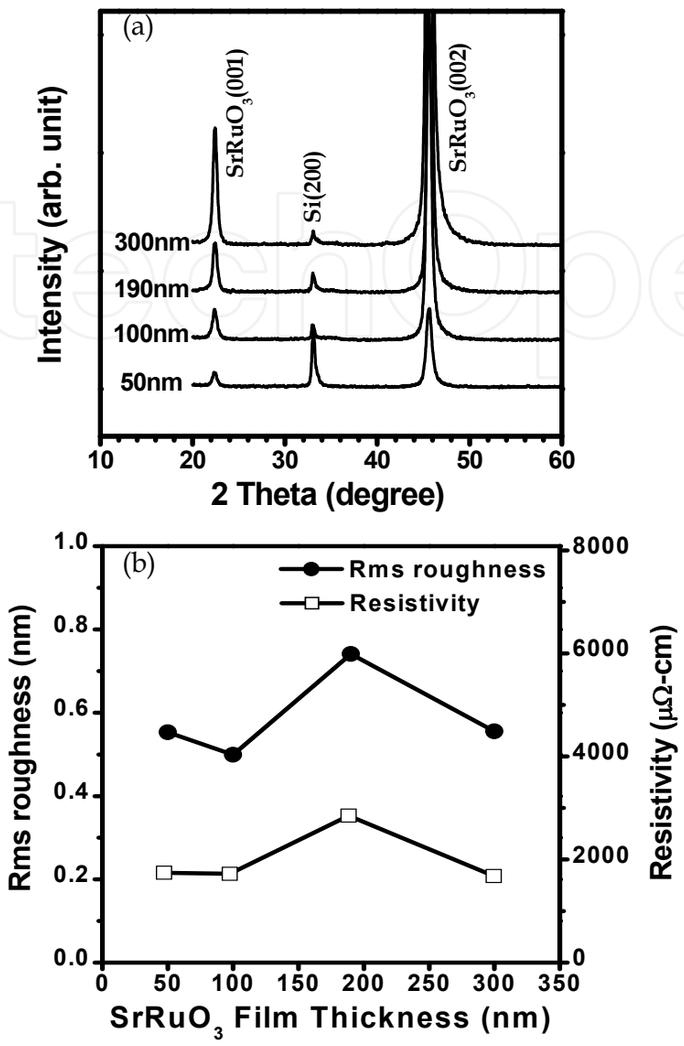

Fig. 3. (a) XRD patterns, (b) rms roughness and resistivity of the $SrRuO_3$ films deposited on 6nm-thick SrO buffer layers as a function of $SrRuO_3$ thickness

Figure 4(a) and 4(b) show XRD patterns and variation of rms roughness and resistivity, respectively, for 190nm-thick $SrRuO_3$ films as a function of $SrRuO_3$ deposition temperature. As shown in Fig. 4(a), $SrRuO_3$ films deposited at 550 and 600°C show $SrRuO_3$ (110) peaks in addition to the $SrRuO_3${001} peaks. This indicates that the films deposited at lower temperatures exhibit a polycrystalline nature rather than an epitaxial relationship. The $SrRuO_3$ (110) peak disappears in the films deposited above 650°C and the films are grown with an epitaxial relationship with Si (001) substrates. As shown in Fig. 4(b), the rms roughness of the films continuously increases with increasing deposition temperature, and a rms roughness of 7.4 Å is noted in the films deposited at 650°C. The rms roughness of the $SrRuO_3$ films deposited on SrO/Si substrates is higher than that of the films deposited on $SrTiO_3$ single crystals [13]. In the $SrRuO_3$/SrO/Si structure, even though the films deposited above 650°C were epitaxially grown, the high rms roughness of the $SrRuO_3$ films was

attributed to the unstable interface structure of SrO/Si, compared with the $SrTiO_3$ single crystal substrate. The resistivity of the $SrRuO_3$ films abruptly decreases as the deposition temperature increases up to 650°C and maintains a constant value of about 1700 μΩ-cm at deposition temperatures above 650°C.The $SrRuO_3$ films grown with an epitaxial relationship exhibit lower resistivity than the polycrystalline films.

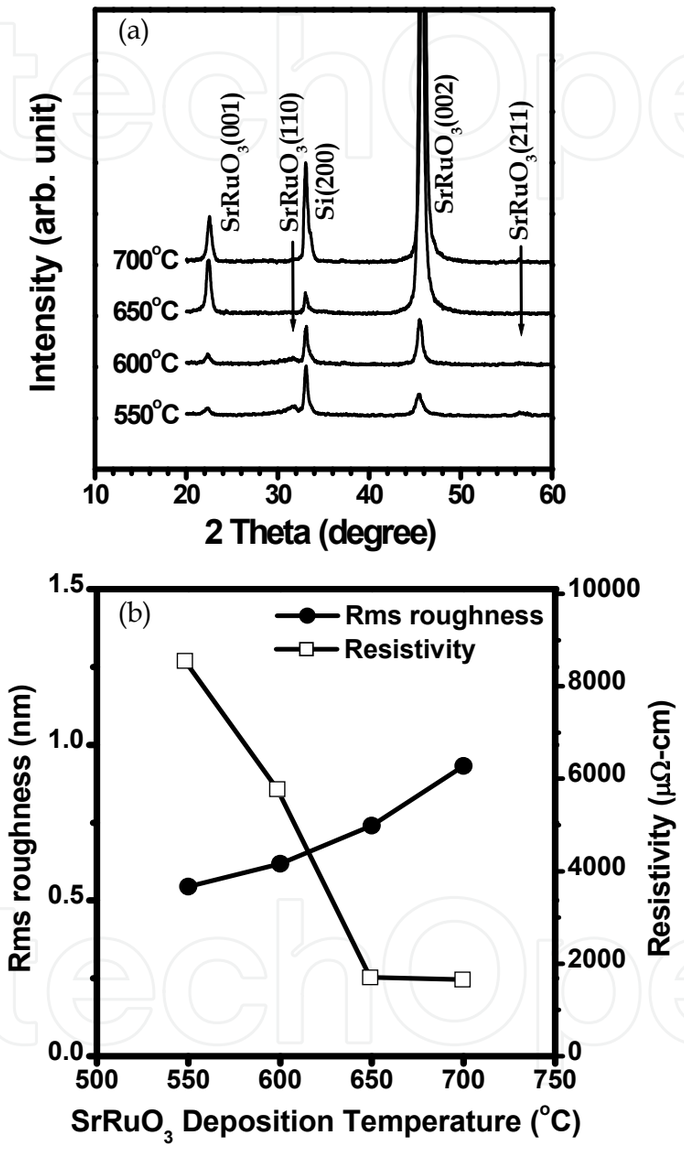

Fig. 4. (a) XRD patterns and (b) rms roughness and resistivity of the $SrRuO_3$ films deposited on 6nm-thick SrO buffer layers as a function of $SrRuO_3$ deposition temperature

Figure 5 shows the RBS spectrum of 190 nm thick-$SrRuO_3$ films deposited at 650°C on SrO/Si substrates. The compositions of Sr and Ru in the $SrRuO_3$ films deposited from stoichiometric $SrRuO_3$ targets are Sr/(Sr+Ru) = 50.52 % and Ru/(Sr+Ru) = 49.48 % from the RBS analysis. Because the Sr and Ru elements are overlapped, the composition of the films

was fitted by repeated adjustments with the standard composition of $SrRuO_3$. The results suggest that the epitaxial $SrRuO_3$ films deposited by pulsed laser deposition show the same composition as $SrRuO_3$ targets.

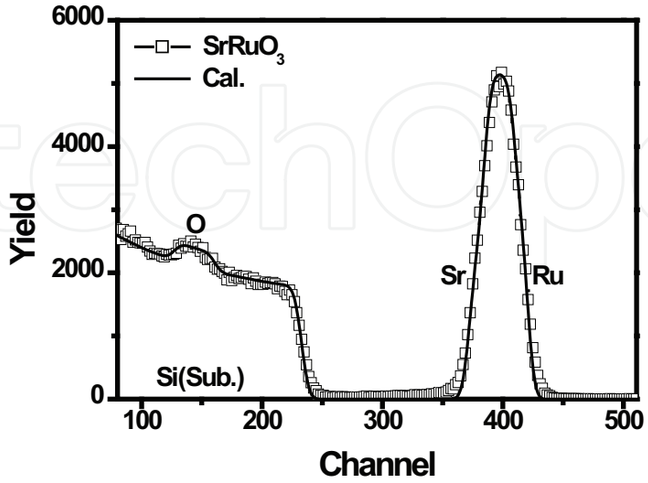

Fig. 5. RBS spectrum of 190nm-thick $SrRuO_3$ films deposited at 650°C on SrO/Si substrates

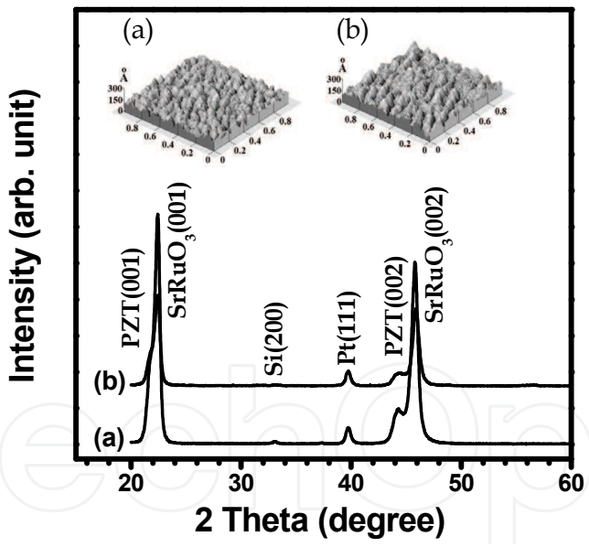

Fig. 6. XRD patterns of PZT thin films deposited at (a) 575°C and (b) 600°C on 190nm-thick $SrRuO_3$ films. The insets show three-dimensional AFM images of PZT films deposited at (a) 575°C and (b) 600°C

Figure 6 shows XRD patterns of 100 nm thick-$Pb(Zr_{0.2}Ti_{0.8})O_3$ (PZT) films deposited at 575 and 600°C on epitaxial $SrRuO_3$/SrO/Si substrates. The (a) and (b) in inset of Fig. 6 show three dimensional AFM images of PZT films deposited at 575°C and 600°C, respectively. The rms roughness of the PZT films deposited at 575 and 600°C are approximately 23Å and 26Å, respectively. The PZT films, as revealed in the XRD patterns of Fig. 6, exhibit a close

relationship with $SrRuO_3${001} at deposition temperatures of 575 and 600°C. The Pt (111) peak originates from the top electrode in the Pt/PZT/$SrRuO_3$/SrO/Si capacitor structures. However, the peak intensities of PZT{001} decrease with increasing deposition temperature. The PZT films react with the $SrRuO_3$ bottom electrode at high deposition temperature, resulting in Pb diffusion into the $SrRuO_3/SrTiO_3$ [15]. Even though Pb is diffused into the $SrRuO_3$ films, PZT films deposited on $SrRuO_3/SrTiO_3$ exhibit a good epitaxial relationship maintaining the predominating crystallinity. In order to investigate the distributions of each element in the PZT films deposited on $SrRuO_3$/SrO/Si, the elemental distribution in each layer was analyzed by secondary ion mass spectroscopy (SIMS), as shown in Fig. 7 (a). The Pb from the PZT films deposited at 600°C was clearly observed within the $SrRuO_3$ layer, indicating similar diffusion behavior of Pb into the $SrRuO_3/SrTiO_3$ [15]. In addition, silicon was also observed at the PZT layer as well as at the $SrRuO_3$ layer. The silicon existing in the PZT and $SrRuO_3$ films will present as silicon oxide, because silicon oxide phase is thermodynamically stable compared with Si element. The silicon oxide will exert a harmful influence upon the crystallinity and the morphologies of the PZT films. The existence of silicon in the PZT layer and Pb in the $SrRuO_3$ layer was also verified by the AES depth-profile as shown in Fig. 7(b). A phi-scan was performed to identify whether the PZT films are epitaxially grown on the $SrRuO_3$ films. From the results (not shown here), PZT films do not exhibit epitaxial growth on the $SrRuO_3$ bottom electrode. The PZT films were only grown with (00l) preferred orientation on $SrRuO_3$ electrodes. From the ω-scan of the PZT films deposited at 575°C, the FWHM value of the PZT (002) is approximately 7.08°. Thus, the crystalline quality of the PZT films deposited on $SrRuO_3$/SrO/Si was distinctly influenced by the silicon oxide within the PZT layers.

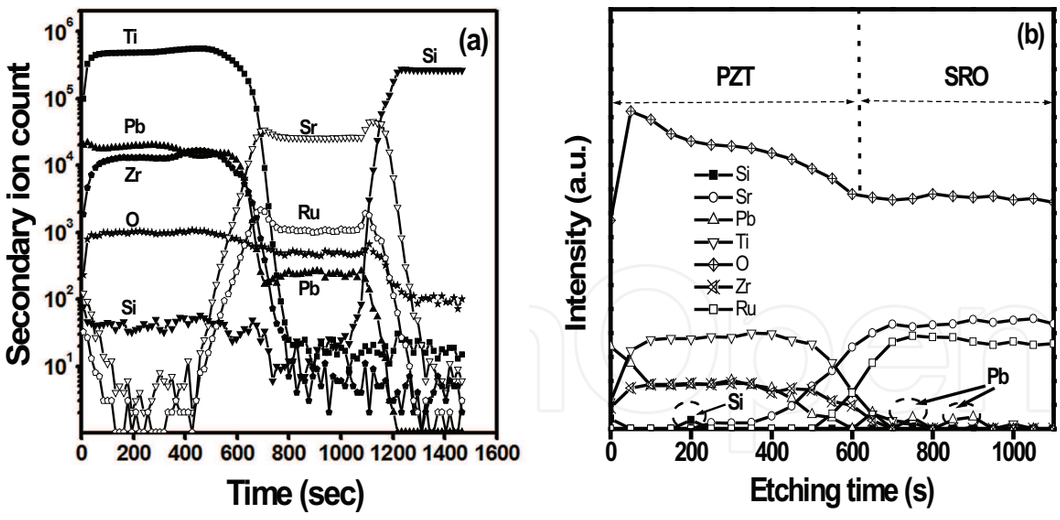

Fig. 7. (a) SIMS and (b) AES depth-profiles of PZT (100nm) films deposited at 600°C on $SrRuO_3$/SrO/Si

Figures 8(a) and 8(b) show P-E hysteresis loops and leakage current densities, respectively, as a function of applied voltage in 100 nm thick-PZT films deposited at 575 and 600°C. The PZT films deposited at both temperatures show similar P-E hysteresis loops, and were polycrystalline nature. The $2P_r$ (remanent polarization) and E_c (coercive field) of the PZT films are approximately 40 μC/cm² and 100 kV/cm, respectively. The lower P_r values

relative to reported values may be due to the poor crystallization of the PZT films resulting from inclusion of silicon oxide phase. As shown in Fig. 8(b), leakage current densities of the PZT films deposited at 575°C are approximately 2×10^{-7} A/cm² at 1 V. The breakdown strength of the films was approximately 150kV/cm. The lower breakdown strength of the films may be due to the rough surface morphologies, as shown in the inset of Fig. 6.

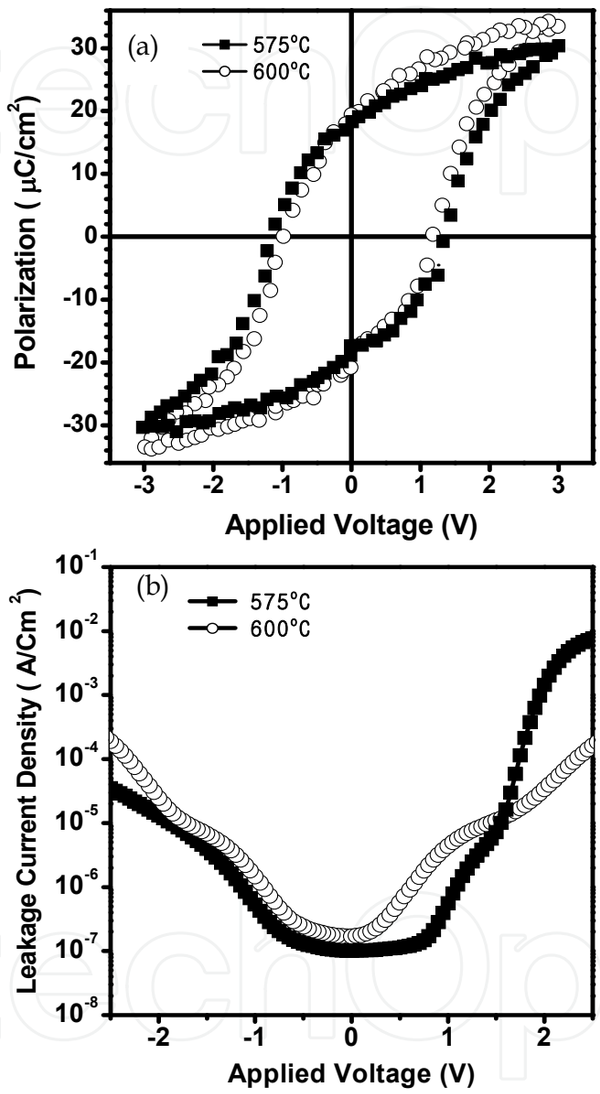

Fig. 8. (a) P-E hysteresis loops and (b) leakage current densities of 100nm thick-PZT thin films deposited at 575°C and 600°C

4. Conclusions

$SrRuO_3$ bottom electrodes were grown with an epitaxial relationship with SrO buffered-Si(001) substrates by pulsed laser deposition. The structural and electrical properties of the $SrRuO_3$ films were studied with deposition parameters of $SrRuO_3$ on the optimized SrO

buffer layered Si (001) substrates. The optimum conditions of SrO buffer layers for $SrRuO_3$ preferred growth were a deposition temperature of 700°C, deposition pressure of 1×10^{-6} Torr, and thickness of 6 nm. 100nm thick-$SrRuO_3$ bottom electrodes deposited at 650°C on SrO buffered-Si(001) substrates showed a rms roughness of approximately 5.0 Å and a resistivity of 1700 μΩ-cm. 100nm thick-$Pb(Zr_{0.2}Ti_{0.8})O_3$ thin films deposited at 575°C on $SrRuO_3$/SrO/Si substrates showed a (00*l*) preferred orientation and exhibited a $2P_r$ of 40 μC/cm² and a E_c of 100 kV/cm. The leakage current density of the PZT films was approximately 1×10^{-7} A/cm² at 1 V. The silicon oxide phase, which presents within the PZT and $SrRuO_3$ films, influences the crystallinity of the PZT films and the resistivity of the $SrRuO_3$ electrodes.

5. Acknowledgments

This research was funded by the Center for Ultramicrochemical Process Systems sponsored by KOSEF, through a Korea Science and Engineering Foundation(KOSEF) grant funded by the Korean government (MOST) (R01-2007-000-21017-0), and was also supported by the BK 21 project.

6. References

[1] J.F. Scott, Ferroelectric memories, Vol. 3 of the Springer series on *Advanced Microelectronics*, Springer, Heidelberg, April 2000.
[2] T. Hidaka, T. Mayurama, M. Saitoh, N. Mikoshiba, M. Shimizu, T. Shiosaki, L.A. Wills, R. Hiskes, S.A. Dicarolis, and J. Amano, *Appl. Phys. Lett*. 68, 1996, 2358.
[3] M.E. Lines and A.M. Glass, *Principles and Applications of Ferroelectrics and Related Materials*, Oxford University Press, Oxford, England, 1977, p. 525.
[4] W.S. Lee, K.C. Ahn, C.S. Kim, and S.G. Yoon, *J. Vac. Sci. Technol*. B 23 (2005) 1901.
[5] W.S. Lee, K.C. Ahn, H.J. Shin, Y.S. Kim, K.S. No, and S.G. Yoon, *Integr. Ferroelectr*. 73 (2005) 125.
[6] C.B. Eom, R.J. Cava, R.M. Fleming, J.M. Phillips, R.B. VanDover, J.H. Marshall, J.W.P. Hsu, J.J. Krajewski, and W.F. Peck Jr., *Science*, 258 (1992) 1766.
[7] P. Legagneux, G. Garry, D. Dieumegard, C. Schwebel, C. Pellet, G. Gautherin, and J. Siejka, *Appl. Phys. Lett.* 53 (1988) 1506.
[8] D.K. Fork, D.B. Fenner, G.A.N. Connell, J.M. Phillips, and T.H. Geballe, *Appl. Phys. Lett*. 57 (1990) 1137.
[9] D.K. Fork, F.A. Ponce, J.C. Tramontana, and T.H. Geballe, *Appl. Phys. Lett*. 58 (1991) 2294.
[10] Y. Kado and Y. Arita, *J. Appl. Phys*. 61 (1987) 2398.
[11] S.K. Singh and S.B. Palmer, *Ferroelectrics*, 328 (2005) 85
[12] T. Higuchi, Y. Chen, J. Koike, S. Iwashita, M. Ishida, and T. Shimoda, *Jpn. J. Appl. Phys*. 41 (2002) 6867.
[13] W.S. Lee, K.C. Ahn, and S.G. Yoon, *J. Vac. Sci. Technol*. B 23 (2005) 1901.
[14] Q.X. Jia, F. Chu, C.D. Adams, X.D. Wu, M. Hawley, J.H. Cho, A.T. Findikoglu, S.R. Foltyn, J.L. Smith, and T.E. Mitchell, *J. Mater. Res*. 11 (1996) 2263.
[15] W.S. Lee, G.H. Jung, D.H. Kim, S.W. Kim, H.J. Kim, J.R. Park, Y.P. Song, H.K. Yoon, S.M. Lee, I.H. Choi, and S.G. Yoon, *J. of KIEEME*, 18 (2005) 810.

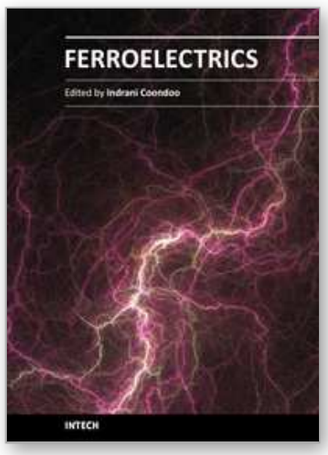

Ferroelectrics
Edited by Dr Indrani Coondoo

ISBN 978-953-307-439-9
Hard cover, 450 pages
Publisher InTech
Published online 14, December, 2010
Published in print edition December, 2010

Ferroelectric materials exhibit a wide spectrum of functional properties, including switchable polarization, piezoelectricity, high non-linear optical activity, pyroelectricity, and non-linear dielectric behaviour. These properties are crucial for application in electronic devices such as sensors, microactuators, infrared detectors, microwave phase filters and, non-volatile memories. This unique combination of properties of ferroelectric materials has attracted researchers and engineers for a long time. This book reviews a wide range of diverse topics related to the phenomenon of ferroelectricity (in the bulk as well as thin film form) and provides a forum for scientists, engineers, and students working in this field. The present book containing 24 chapters is a result of contributions of experts from international scientific community working in different aspects of ferroelectricity related to experimental and theoretical work aimed at the understanding of ferroelectricity and their utilization in devices. It provides an up-to-date insightful coverage to the recent advances in the synthesis, characterization, functional properties and potential device applications in specialized areas.

InTech Europe
University Campus STeP Ri
Slavka Krautzeka 83/A
51000 Rijeka, Croatia
Phone: +385 (51) 770 447
Fax: +385 (51) 686 166
www.intechopen.com

InTech China
Unit 405, Office Block, Hotel Equatorial Shanghai
No.65, Yan An Road (West), Shanghai, 200040, China
中国上海市延安西路65号上海国际贵都大饭店办公楼405单元
Phone: +86-21-62489820
Fax: +86-21-62489821

IntechOpen